

## Article

# Anchoring Monodispersed NiSe@Ni Particles on Graphene for Energy Storage in Supercapacitors

Xianbin Xiao <sup>1,†</sup>, Fangzhou Jin <sup>1,†</sup>, Zhongsheng Pu <sup>1,\*</sup>, Peng Zhu <sup>1</sup>, Zhiqiang Wei <sup>1</sup>, Hua Yang <sup>1</sup> and Jinlong Jiang <sup>1,2,\*</sup> 

<sup>1</sup> Department of Physics, School of Science, Lanzhou University of Technology, Lanzhou 730050, China; xxianbin29@163.com (X.X.); hyang@lut.edu.cn (H.Y.)

<sup>2</sup> Shandong Laboratory of Yantai Advanced Materials and Green Manufacturing, Yantai 264006, China

\* Correspondence: zhongshengpu@126.com (Z.P.); jinlong@amgm.ac.cn (J.J.)

† These authors contributed equally to this work.

**Abstract:** In this study, monodispersed NiSe@Ni particles were successfully anchored on graphene sheets by electroless nickel plating combined with a chemical-vapor-reaction process, in which the nickel particles were first deposited onto graphene sheets and subsequently transformed in situ into NiSe@Ni at an elevated temperature. The obtained product showed a unique multi-dimensional coupling structure, namely, monodispersed NiSe@Ni particles (0 D) anchored on graphene sheets (2 D), which enabled maximum synergy on the specific surface area, conductivity, and the electrochemical activity of NiSe, Ni, and graphene multi-phases. The NiSe@Ni/graphene composite showed a specific capacity of 302 mAh g<sup>-1</sup> at a current density of 1 A g<sup>-1</sup> in a potassium-hydroxide-electrolyte solution. Meanwhile, the hybrid supercapacitor of NiSe@Ni/graphene//AC exhibited a high energy density of 68.0 Wh kg<sup>-1</sup> at 803.0 W kg<sup>-1</sup> and maintained 72.53% of the initial capacity after 10,000 cycles at a current density of 10 A g<sup>-1</sup>.

**Keywords:** monodispersed particles; graphene; selenide nickel; hybrid supercapacitor



**Citation:** Xiao, X.; Jin, F.; Pu, Z.; Zhu, P.; Wei, Z.; Yang, H.; Jiang, J.

Anchoring Monodispersed NiSe@Ni Particles on Graphene for Energy Storage in Supercapacitors. *Coatings* **2023**, *13*, 885. <https://doi.org/10.3390/coatings13050885>

Academic Editors: Dimitrios Tasis and Gianfranco Carotenuto

Received: 12 March 2023

Revised: 9 April 2023

Accepted: 6 May 2023

Published: 8 May 2023



**Copyright:** © 2023 by the authors. Licensee MDPI, Basel, Switzerland. This article is an open access article distributed under the terms and conditions of the Creative Commons Attribution (CC BY) license (<https://creativecommons.org/licenses/by/4.0/>).

## 1. Introduction

The exploration of renewable energy sources and the creation of sustainable energy-storage solutions have become a highly active research areas [1–3]. Supercapacitors have garnered significant attention as potential energy-storage systems due to their high power density, rapid charging and discharging capabilities, extended lifespan, and eco-friendliness [4]. The demand for high-performance energy-storage systems underscores the urgent need to design advanced electrode materials. The inherently low energy density of conventional supercapacitors greatly restricts their potential applications. As a result, the assembly of asymmetric supercapacitors with two dissimilar electrode materials provides the clear advantage of expanded operational voltage range, which greatly enhances energy density [5]. In recent years, the main electrode materials used for supercapacitor applications included carbon materials [6] and transition-metal oxides [7], hydroxides [8], and sulfides [9], along with their composites. Graphene has a two-dimensional structure, consisting of a single layer of sp<sup>2</sup> hybridized carbon atoms arranged in a honeycomb lattice [10]. Its remarkable electronic properties make it a highly promising and noteworthy material for use in supercapacitors, owing to its extraordinary properties, such as its high electrical conductivity (6000 S cm<sup>-1</sup>) and surface area (2675 m<sup>2</sup> g<sup>-1</sup>) [11]. According to Zhang et al., pristine graphene exhibits an electrical double-layer capacitance of 21 mF cm<sup>-2</sup>, leading to a theoretical specific capacitance of 550 F g<sup>-1</sup>, assuming full utilization [12]. Karaman et al. managed to enhance the capacitive performance of GO by controlling and enhancing its surface-nitrogen content and surface morphology. This resulted in an impressive energy density of 39 Wh kg<sup>-1</sup> in an acidic electrolyte of 0.1 A g<sup>-1</sup> [13].

A commonly accepted notion is that electrodes' electrochemical performances can be improved by utilizing large-area materials, or by enlarging their surface area [14]. These approaches can augment the interfacial region between the electrode and the electrolytic solution, consequently enhancing the energy-storage capacity of the electrode. Furthermore, increasing the specific surface area can diminish the charge density of the electrode, leading to better cycle stability and prolonged service life [15]. Although it is a practical technique to increase the specific surface area and active sites by integrating different materials with diverse structures, volumes, and areas, the significant agglomeration phenomenon that occurs during the compounding process creates dead volume by taking part in the electrochemical reaction, which cannot be overlooked [16]. Transition-metal selenides are excellent candidates for supercapacitors due to their high theoretical capacitance, metallic character, exceptional electrical conductivity, and good reversibility [17]. Nanoscale Ni<sub>3</sub>Se<sub>2</sub> on nickel foam was produced by Zhao et al., demonstrating excellent rate capability and a capacitance of 1234 F g<sup>-1</sup> [18]. Furthermore, Bai et al. successfully fabricated a two-phase nickel-selenide-nanoparticle electrode material with outstanding performance, exhibiting a capacity of 669 C g<sup>-1</sup> [19]. While selenide-related composite materials have extensive potential in energy storage, since the agglomeration phenomenon that arises during the preparation process is challenging to circumvent, the improvements in the energy-storage performance have fallen short of expectations.

We synthesized NiSe@Ni/graphene composites through a novel preparation method involving the embedding of metallic nickel particles on graphene sheets to form convex contacts, followed by the calcination of precursors and selenium powders via chemical-vapor deposition under an inert gas. This method effectively prevents large-area agglomeration during NiSe nucleation, resulting in a composite material that combines 2D flake graphene with monodisperse 3D NiSe particles. The presence of metallic nickel in the composite serves as a bridge, resulting in a multicomponent structure with a higher specific surface area, more active sites, and easier channels for ion diffusion. The electrochemical performance of the composite is significantly improved, as evidenced by our results.

## 2. Experimental Methods

### 2.1. Chemicals and Reagents

The Harbin Institute of Technology was the source of the graphene used in this study. Other reagents, namely C<sub>6</sub>H<sub>5</sub>Na<sub>3</sub>O<sub>7</sub>·H<sub>2</sub>O, PbCl<sub>2</sub>, SnCl<sub>2</sub>, NaH<sub>2</sub>PO<sub>2</sub>·H<sub>2</sub>O, and C<sub>12</sub>H<sub>25</sub>SO<sub>4</sub>Na, were procured from Yantai Shuang Chemical Reagent Co., Ltd. (Yantai, China).

### 2.2. Surface Pretreatment of Graphene

An electroless plating method was utilized to produce nickel-coated graphene sheets (Ni/graphene). Graphene sheets obtained by the liquid-phase exfoliation method are highly chemically inert. The graphene sheets underwent a three-step treatment process consisting of acid oxidation, sensitization, and activation prior to the nickel deposition [20]. A total of 0.4 g of graphene was mixed with a solution of 30 mL nitric acid and 10 mL sulfuric acid. After 1 h of sonication, the mixture was heated for 5 h at 80 °C in a water bath. The pH of the samples was adjusted to 7, and they were washed with deionized water. To reduce the oxygen functional groups on graphene oxide to organic functional groups, such as hydroxyl and carbonyl groups, graphene oxide and 10 g SnCl<sub>2</sub> were combined in 0.12 M hydrochloric acid. After ultrasonic stirring for 20 min, the sample was repeatedly washed with deionized water until the pH value was 7 to obtain sensitized graphene. Finally, sensitized graphene and 0.05 g PbCl<sub>2</sub> were mixed in 0.24 M hydrochloric acid, and stirred under ultrasound for 20 min to form lead catalyst core on the surface of graphene. The samples were washed with deionized water to pH 7 and dried at 60 °C for 12 h to obtain pretreated graphene.

### 2.3. Preparation of Ni/Graphene

The Ni/graphene were prepared according to a modified method [21]. Firstly, 3 g  $\text{NiSO}_4 \cdot 6\text{H}_2\text{O}$  and 7.2 g  $\text{NH}_4\text{Cl}$  were dispersed in 100 mL of deionized water. Next, 1.8 g  $\text{NaH}_2\text{PO}_2$ , 2 g  $\text{C}_6\text{H}_5\text{Na}_3\text{O}_7$ , and 0.5 mg  $\text{C}_{12}\text{H}_{25}\text{SO}_3\text{Na}$  were added to the mixed solution in sequence. During the process,  $\text{Ni}^{2+}$  ions were reduced to metallic nickel through a redox reaction catalyzed by the highly reducing  $\text{NaH}_2\text{PO}_2$ , which was immobilized on the pretreated graphene. The main reactions in electroless plating bath were as follows:



As a complexing agent,  $\text{C}_6\text{H}_5\text{Na}_3\text{O}_7$  improves the dispersion and coverage of metallic nickel [22]. The  $\text{C}_{12}\text{H}_{25}\text{SO}_3\text{Na}$  (SDS) is an anionic surfactant, which improves the adsorption capacity of metallic nickel on the surface of graphene and prevents the formation of pinholes on its surface, as well as the generation of  $\text{H}_2$  [23]. The solution was simplified by vigorously stirring in  $\text{NH}_3 \cdot \text{H}_2\text{O}$  solution until the pH value reached 10. Next, the pretreated graphene was introduced into the solution, which was then transferred into an oil bath and heated at  $85^\circ\text{C}$  for 15 h. Once the reaction had finished, the mixture was allowed to cool to room temperature, and the resulting powders were gathered by high-speed centrifugation and washed with de-ionized water until a neutral pH was achieved. The sample powder was placed in a drying oven at a constant temperature of  $60^\circ\text{C}$ , with a pressure of 0.06 MPa, for 12 h.

### 2.4. Preparation of NiSe@Ni/Graphene

Based on theoretical calculations, the synthesis of NiSe required 100 mg of selenium powder. However, during the nickel-selenide experiments, selenium powder occurred in a gaseous state at  $700^\circ\text{C}$ , leading to a significant loss of gaseous selenium powder in the vacuum tube with high flow rate, which did not participate in the reaction. Therefore, we added 0.4 g of selenium (Se) powder in the upstream ceramic boat and 100 mg of Ni/graphene in the downstream ceramic boat [24]. Under the protection of inert gas, the powder was heated at  $700^\circ\text{C}$  (increase rate:  $10^\circ\text{C min}^{-1}$ ) for 1 h. A further NiSe@Ni/graphene composite was generated after natural cooling to room temperature. The production process of the NiSe@Ni/graphene is illustrated in Figure 1.

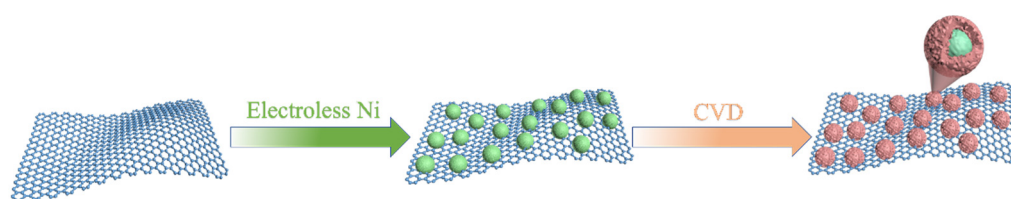


**Figure 1.** A diagrammatic representation of the process for producing NiSe@Ni/graphene.

### 2.5. Characterization of Materials

The structural characterization of the composites was performed using XRD (Bruker D8, ADVANCE, Billerica, MA, USA) with  $\text{Cu K}\alpha$  radiation ( $\lambda = 1.54178 \text{ \AA}$ ). The elemental composition of the composites was analyzed using XPS (AXIS Supra, Thermo Fisher Scientific Inc., Walsham, MA, USA) with monochromatic  $\text{Al K}\alpha$  radiation. Identification of chemical constituents in composites was carried out using a Raman spectrometer with an excitation wavelength of 532 nm (Lab RAM HR Evolution, HORIBA Jobin Inc., Paris, France). The SEM (JSM-6701F, JEM2010, JEOL Ltd., Tokyo, Japan) and TEM (TF20, JEOL Ltd., Tokyo, Japan) were used to observe the specific appearance and structural features of the composite samples.

### 2.6. Electrochemical Measurements

An electrochemical analysis was conducted using a CS350H work-station from Wuhan Corrtest Instrument, China. The performance test utilized a three-electrode configuration, in which the active material served as the working electrode, platinum foil acted as the counter electrode, and Ag/AgCl served as the reference electrode. A 2-M KOH aqueous solution was used as the electrolyte, and the test was carried out at room temperature. The active material was evenly spread on the surface of foamed nickel ( $1 \times 1.5 \text{ cm}^2$ ) in a ratio of active materials (2.0 mg):super P:PVDF = 8:1:1 after thorough mixing. The specific capacitance ( $Q, \text{mAh g}^{-1}$ ) of the sample was calculated using the electrochemical test results and the following formula [25]:

$$Q = \frac{\int_0^{\Delta t} I dt}{m} \quad (2)$$

The constant discharging current and constant discharge time, along with the mass of active material, are denoted by the symbols  $I$ ,  $\Delta t$ , and  $m$ , respectively.

For the hybrid capacitor, the composite material (1.0 mg) and activated carbon (AC, 5.0 mg) in 2-M KOH aqueous solution were used as positive and negative electrodes, respectively, to assemble a coin cell. Calculation according to formula of energy and power density [26]:

$$E = \frac{I \int V dt}{3.6 \times m} \quad (3)$$

$$P = \frac{3600 \times E}{\Delta t} \quad (4)$$

The variables in the equation above are as follows: the current of discharge ( $I$ ), the working potential ( $V$ ), the time of discharge ( $t$ ), and the mass ( $m$ ) of the active material.

## 3. Results and Discussion

### 3.1. Morphology Analysis

Figure 2a,b display the SEM of the Ni/graphene composites. It can be seen that due to the reduction of the  $\text{NaH}_2\text{PO}_2$  and the action of the anionic surfactant,  $\text{C}_{12}\text{H}_{25}\text{SO}_3\text{Na}$ , 50-nm metallic nickel particles were firmly attached to a sleek graphene surface through anchoring. Although the complexing agent,  $\text{C}_6\text{H}_5\text{Na}_3\text{O}_7$ , can enhance the dispersion of metallic nickel, it can still be seen that part of the metallic nickel was agglomerated on the graphene surface. This phenomenon limited the charge-transport efficiency. When the sample was selenized at a high temperature, the nickel layer of graphene gradually transformed into NiSe, which wrapped around the metallic nickel to form a NiSe@Ni. As shown in Figure 2c,d, when the Ni/graphene was selenized by the chemical-vapor deposition, the metal nickel on the graphene surface had obvious agglomeration before selenization, but the agglomeration was obviously weakened after the selenization. The NiSe nanoparticles with rough surfaces and an average diameter of 180–210 nm were uniformly immobilized onto the surface of the graphene, thereby forming a NiSe@Ni/graphene composite material. The anisotropic growth of the NiSe@Ni/graphene increased the particle size and surface area, leading to more active sites. The nucleation of the NiSe particles uniformly dispersed on the graphene surface provided an excellent interface structure and improved the electron-transfer efficiency. A strong explanation was therefore provided for the enhanced electrochemical performance. It can be seen from the HRTEM images (Figure 2c,d) that the surfaces of the graphene sheets were roughened by the immobilization of a substantial quantity of NiSe particles onto them. The lattice fringes with interlayer distances of 0.27 and 0.2 nm in the HRTEM (Figure 2c) correspond to the (101) and (001) planes of the NiSe particles. The corresponding SAED pattern (Figure 2d) presented discrete diffraction spots, representing multiple facets of the NiSe structure, including (101), (102), (110), and the cubic Ni (111) plane (PDF # 04-0850). The distribution of the elements in the sample is shown in

Figure 2e. The Ni (green), C (red), and Se (blue) elements were uniformly distributed on the graphene. The EDS shows that the NiSe@Ni/graphene was composed of C, Ni, and Se elements. The observed O and Cu elements were derived from air mixed in the sample preparation and the copper column used in the test sample, respectively [27]. Section 2.4 provides the explanation for the use of excess selenium powder in the samples' preparation. To synthesize the NiSe, only 100 mg of selenium powder was used, despite the requirement of 400 mg for chemical-vapor deposition. This resulted in a different Se-content ratio from that which we expected based on the SEM mapping. In fact, the actual ratio was closer to  $M_{\text{graphene}}:M_{\text{Ni}}:M_{\text{Se}} = 2:3:3$ .

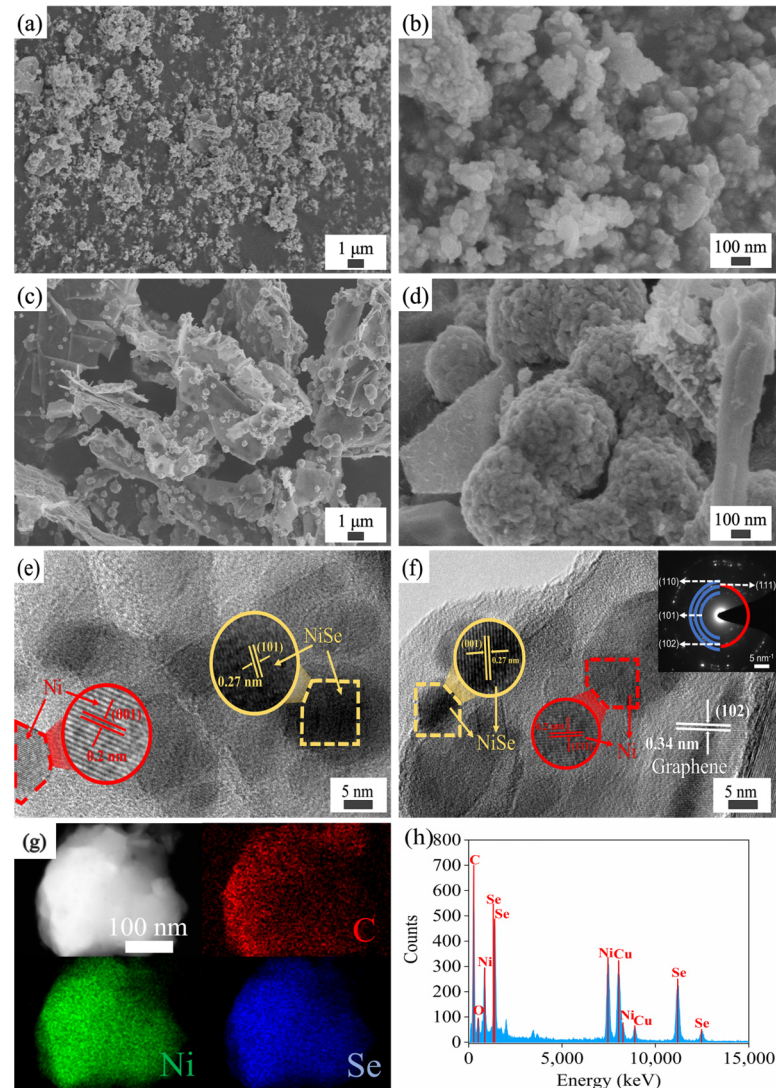


**Figure 2.** (a,b) SEM of Ni/graphene. (c,d) SEM of NiSe@Ni/graphene. (e,f) HRTEM and SAED pattern. (g) Elemental mapping images. (h) EDS energy spectrum.

### 3.2. Phase Analysis

The X-ray diffraction results (Figure 3a) show that the diffraction peaks of the NiSe@Ni/graphene can be accurately identified as originating from the NiSe (JCPDF # 02-0892) and the face-centered cubic Ni (JCPDF # 04-0850). The XRD pattern showed characteristic peaks of Ni/graphene at  $44.5^\circ$ ,  $51.8^\circ$ , and  $76.4^\circ$ , which corresponded to the (111), (200), and (220) planes of the face-centered cubic Ni. These results suggest that the Ni coating exhibited exceptional crystalline properties [24]. After the selenization of the Ni/graphene samples, we can see that the (100), (101), (102), (110), (103), (201), (202),

(004), (203), and (211) corresponded well to the characteristic peaks of the NiSe without extraneous impurity peaks, which suggests that the high-purity nickel-selenide crystals were distributed across the surfaces of the graphene sheets. The crystallite sizes of the Ni/graphene and NiSe@Ni/graphene were calculated using the Debye–Scherrer formula [28], and they were found to be 11.8 nm and 75.0 nm, respectively. The Raman spectrum of the NiSe@Ni/graphene is shown in Figure 3b. The classical D, G, and 2D peaks of the graphene appeared at 1300, 1580, and 2700  $\text{cm}^{-1}$ . The Raman image of the NiSe@Ni/graphene was used to analyze the state of the graphene after the recombination (Figure 3b). As the D band was derived from the vibration of the  $\text{sp}^3$  hybridized carbon atoms present in the disordered domains and defect regions [24], the intensity ratio of the D band to the G band at a high temperature of 700 °C, which was 0.1, indicated the presence of a higher number of defects in the composite sample. This can be advantageous in terms of exposing more active sites and accelerating mass transport during the electrochemical process. In contrast to the single-layer graphene, in which the 2D peak had a single peak form as it was formed by the direct intersection of two equal-energy-band electrons, the 2D peak in the multilayer graphene was a result of the interaction between the layers. As the number of layers increased, the interaction between the layers weakened, resulting in a decrease in the intensity of the 2D peak. Based on these findings, the 2D peak in the single-layer graphene in this study was expected to be more pronounced.

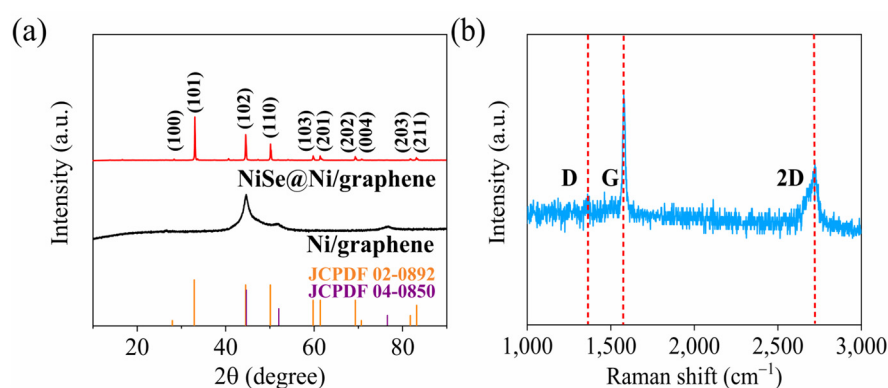
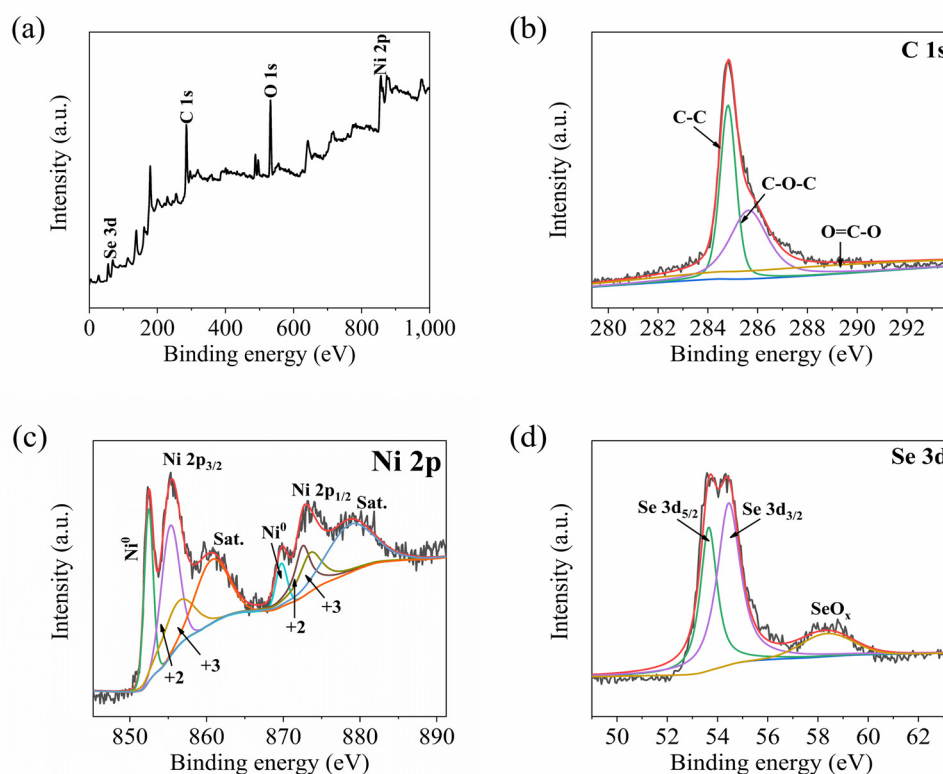


**Figure 3.** (a) XRD of NiSe@Ni/graphene and Ni/graphene. (b) Raman spectra of the graphene of composite sample.

### 3.3. XPS Analysis

The surface-element compositions and chemical states of the NiSe@Ni/graphene composite were analyzed using XPS, as depicted in Figure 4. Based on the survey spectrum of the XPS (Figure 4a), the primary components of the NiSe@Ni/graphene composites were found to be C, Se, and Ni elements. The O 1s peak observed in the spectrum was attributed to contamination resulting from the exposure of the sample to ambient air [29,30]. Figure 4b displays the C 1s spectra that were separated into three distinct peaks, with binding energies of 284.8 eV, 285.5 eV, and 286.7 eV, which corresponded to the C-C, C-O-C, and O=C-O bonds, respectively [31]. The XPS spectrum of the Ni 2p in Figure 4c indicates the presence of Ni 2p<sub>3/2</sub> and Ni 2p<sub>1/2</sub>, as well as their associated satellite peaks [32]. The weak peaks observed at 856.4 eV and 873.7 eV were identified as the Ni<sup>3+</sup> in Ni<sub>3</sub>Se<sub>4</sub>, while the sharp peaks at 855.3 eV and 872.6 eV were identified as the Ni<sup>2+</sup> in the NiSe. Furthermore, the intense peaks at 861.1 eV and 878.8 eV were observed as shakeup satellites for the Ni 2p<sub>3/2</sub> and Ni 2p<sub>1/2</sub> levels (represented as “Sat.” in the spectrum) [33]. Notably, the characteristic peaks observed at 852.5 eV and 869.8 eV originated in the metallic nickel, which provides solid evidence for metallic nickel as an effective medium for ion transport between graphene and NiSe. The peaks deconvoluted at binding energies of 53.61 eV and 54.47 eV can be attributed to the Se 3d<sub>5/2</sub> and Se 3d<sub>3/2</sub> spin-orbit levels of the Se-Ni in the NiSe, respectively. This suggests that chemical bonding occurred between the NiSe

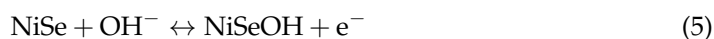
particles and the graphene sheets with large surface areas [34]. The peaks centered at 58.4 eV represent the related oxides of the Se [35].



**Figure 4.** XPS spectra of NiSe@Ni/graphene. (a) XPS full-scan; (b) C 1s; (c) Ni 2p; (d) Se 3d.

### 3.4. Electrode-Electrochemical-Performance Test

We tested the electrochemical performance of the NiSe@Ni/graphene and Ni/graphene in a three-electrode configuration, with KOH as an electrolyte. Figure 5a,c show the CV curves of the NiSe@Ni/graphene and Ni/graphene at the same scan speed ( $50 \text{ mV s}^{-1}$ ) and different scan speeds ( $5\text{--}50 \text{ mV s}^{-1}$ ). Based on the observations in Figure 5a, it can be concluded that the integral area of the CV curve showed an increase within the voltage range of  $-0.2\text{--}0.6 \text{ V}$  for the NiSe@Ni/graphene composite, and that the peak current of this composite was larger than that of the pristine Ni/graphene with similar mass. These findings indicate that the hybrid electrode of the NiSe@Ni/graphene composite exhibited a greater charging-storage capacity and higher specific capacitance. Furthermore, the NiSe@Ni/graphene hybrid electrode displayed almost no shift in the reduction in the potential peak compared to the pristine NiSe electrode. A slight shift was observed in the oxidation-potential peak, but it was very minor. This can be attributed to the fact that the NiSe@Ni/graphene hybrid electrode had a lower internal resistance, resulting in a more reversible redox reaction. The results obtained from the GCD measurements at a current density of  $1 \text{ A g}^{-1}$  (Figure 5b) support this conclusion, and the larger capacity area obtained from the GCD curve was consistent with the results obtained from the CV curve. Finally, Figure 5c shows the CV curves of the NiSe@Ni/graphene composite in a potential window of  $-0.2\text{--}0.6 \text{ V}$  for scanning rates in the range of  $10\text{--}50 \text{ mV s}^{-1}$ . The apparent reduction and oxidation reactions observed in the CV image suggest that the conversion of the nickel ions between the different oxidation states can be attributed to the faradic reaction [24,33,36]. The electron-transfer-construction processes were:



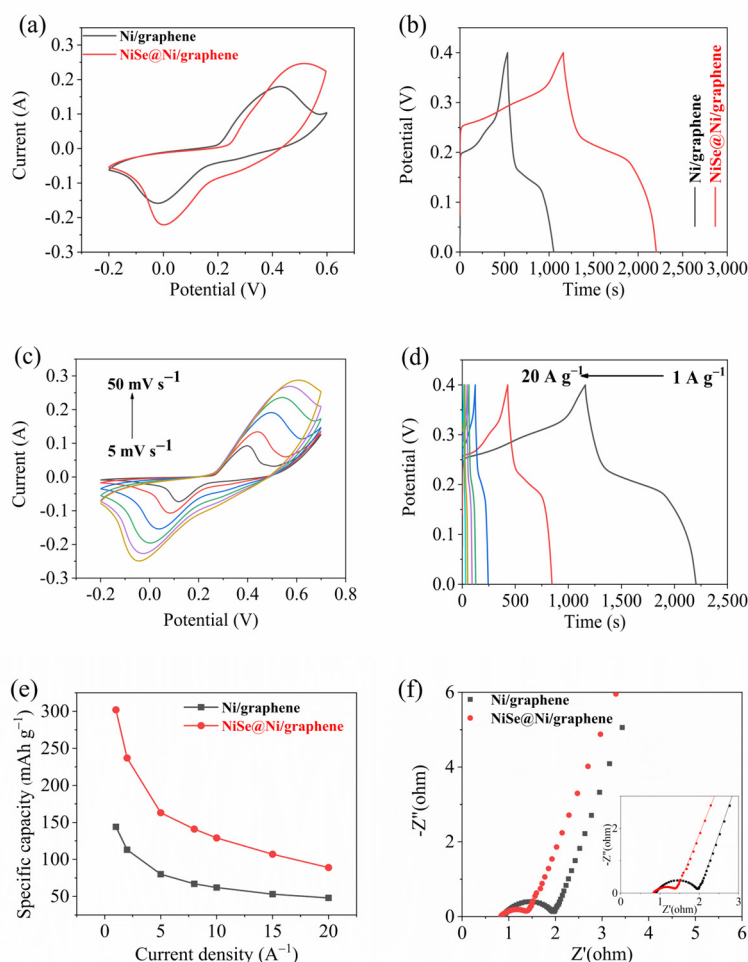
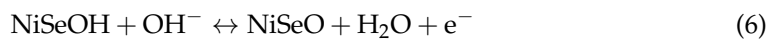


**Figure 5.** (a) CV curves. (b) GCD curves. (c) CV curves of NiSe@Ni/graphene at different scan rates. (d) The changes in GCD curves of NiSe@Ni/graphene under varying current densities. (e) Specific capacities. (f) Nyquist plots.

Therefore, we speculate that two-step oxidation reactions occurred during the charge-transfer process: NiSe oxidation to NiSeOH and NiSeOH oxidation to NiSeO. When we plotted the GCD curves for the NiSe@Ni/graphene in the voltage range of 0–0.4 V (Figure 5d), we found that the redox reaction between the electrode material and the electrolyte had excellent reversibility at the same scan rate in Figure 5c [37,38]. Based on the discharge curve, the electrode exhibited specific capacities ranging from 308 to 89 mAh g<sup>-1</sup>, across a current-density range of 1 to 20 A g<sup>-1</sup>. The enhancement of the electroconductivity can be attributed to the increase in the active sites after the selenization, as well as the addition of the graphene. Furthermore, the diffusion of active species was more favorable due to the corresponding increase in the diffusion coefficient [39]. These results significantly surpassed those obtained on transition-metal nickel selenide in recent years (Table S1). The Nyquist plot of the NiSe@Ni/graphene electrode in Figure 5f exhibits a quasi-semicircular shape, along with a straight line. Moreover, in the high-frequency range, both the Ni/graphene and the NiSe@Ni/graphene electrodes exhibited small semicircular shapes, indicating the low interfacial charge transfer resistance of both electrodes [40]. However, compared with the radius of the semicircle of Ni/graphene, the obvious reduction in the semicircle radius of the NiSe@Ni/graphene meant that the charge-transfer resistor of the sample decreased. Therefore, the calculated  $R_s$  and  $R_{ct}$  of the

NiSe@Ni/graphene were  $0.83 \Omega$  and  $0.52 \Omega$ , respectively; these values were lower than those of the Ni/graphene, which were  $0.88$  and  $1.07 \Omega$ . These results suggest that the sample after selenization had lower resistance and better capacitance performance. Therefore, based on the electrochemical tests, we speculated that the reasons for the performance improvement after the selenization were as follows: (a) The number and distribution of active sites on the Ni/graphene surface were altered following the selenization. Resolving the agglomeration issue enabled more inactive areas to be transformed into active sites and exposed, leading to an enhancement in the electrochemical reactions. (b) Moreover, the selenization process induced modifications in the nanostructure of the Ni/graphene surface, whereby not only did the NiSe particles enhance the electrodes' surface area but, furthermore, the novel ternary structure comprising graphene, metallic nickel, and NiSe further amplified the energy-storage capacity.

According to the three-electrode data of the composite sample of NiSe@Ni/graphene, the composite material's total current was the result of two factors: the current generated by the slow diffusion-control process ( $i_{dif}$ ), and the current resulting from the double layer charge at the electrolyte interface caused by the Faraday effect or the current on the exposed electrode surface ( $i_{cap}$ ). Therefore, the capacitive contribution and the diffusion-controlled contribution were calculated according to the following equation [41]:

$$i_v = i_{dif} + i_{cap} = a \times v^b \quad (7)$$

In particular, the  $b$  value was a key parameter in determining the kinetic information about the electrochemical reaction. A value of  $b = 1$  corresponded to the presence of fast surface-redox reactions and charge/discharge processes inherent in EDLCs, and a value of  $b = 0.5$  corresponded to the presence of the peak current responses of battery-type electrodes with strong redox peaks.

The anodic and cathodic peak currents in the NiSe@Ni/graphene electrode had  $b$ -values of  $0.5003$  and  $0.5368$ , respectively, as determined by the linear plots shown in Figure 6a. These values indicated that the NiSe@Ni/graphene exhibited typical battery-type material behavior. The contribution to the total capacity was analyzed using the following formula [42]:

$$i_v = k_1 v + k_2 v^{\frac{1}{2}} \quad (8)$$

where  $k_1 v$  is the role of the surface capacitance and  $k_2 v^{\frac{1}{2}}$  is the contribution of the diffusion-controlled intercalation.

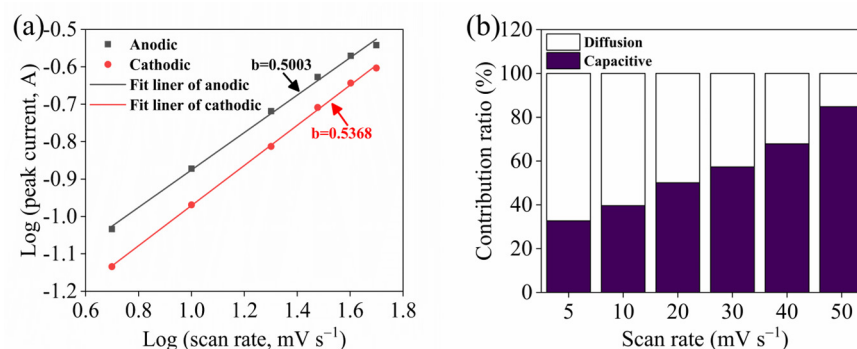


**Figure 6.** (a) The correlation between the logarithm of peak current and the logarithm of scan rates. (b) The percentage of capacitive contribution at different scan rates of the NiSe@Ni/graphene composite.

The surface-capacitance contribution increased, which indicated an increase in the electrodes' surface area. This resulted in more effective reaction areas on the electrode surfaces to accommodate the additional ions. As a result, the distance for ion diffusion between the electrode and the electrolyte was reduced, leading to a decrease in the contribution of the

diffusion current. Moreover, when the surface-capacitance contribution increased, the total capacitance of the electrode also increased, which slowed down the rate of the voltage drop over time [43]. This resulted in more uniform ion diffusion between the electrode and the electrolyte, further reducing the contribution of the diffusion current, as shown in Figure 6b. Based on our experimental results, the excellent electrochemical energy-storage properties of the NiSe@Ni/graphene composite can be attributed to several factors. Firstly, the metal nickel was anchored on the large-area graphene surface and formed a crystal structure with the graphene, introducing lattice-mismatched defects that created more channels for ion diffusion and additional electrochemically active sites. Secondly, the electroless nickel plates encouraged the uniform nucleation of metal selenides and created a novel interfacial structure between the graphene and the NiSe, improving the transport efficiency of the ions and electrons. Thirdly, the selenization reduced the agglomeration of the metallic nickel on the graphene surface, resulting in the even dispersion of the metallic nickel and the NiSe particles. This created more interfaces and pathways for ion diffusion, and adequate room for structural changes during the ion insertion/extraction, along with increased electrode–electrolyte contact. Finally, the introduction of the NiSe particles roughened the electrode surfaces, increasing the valid surface area and capacitance. The specific capacity and the Nyquist curve indicated that the NiSe@Ni/graphene had better conductivity and higher charge-transfer efficiency due to the selenization.

### 3.5. Electrochemical-Performance Test of Hybrid Supercapacitor

Electrochemical investigations were performed on an asymmetric supercapacitor device, specifically NiSe@Ni/graphene||AC, so as to explore the practical applications of the NiSe@Ni/graphene. The electrochemical parameters of the AC electrode are shown in Figure S1 for comparison. The CV graphics of the optimized device were obtained in unequal potential windows, ranging from 0.0–0.9 V to 0.0–1.9 V, revealing distinct anodic and cathodic peaks within the tested voltage range. The redox reaction was sustained even when the operating voltage was raised to 1.7 V. These results demonstrate the practical utility of NiSe@Ni/graphene in this type of device. Figure 7a provides a visual representation of the CV curves. When the voltage continued to rise, the CV curve was obviously deformed, indicating an irreversible reaction [44]. The electrochemical performance of the NiSe@Ni/graphene||AC device remained stable within a potential range of up to 1.6 V. This was demonstrated by the typical CV curves of the device, shown in Figure 7b, which were obtained at scan rates ranging from 5 mV s<sup>-1</sup> to 50 mV s<sup>-1</sup>. Therefore, the NiSe@Ni/graphene||AC ACS device can operate in a potential window of up to 1.6 V for stable electrochemical performance. No obvious distortion was observed in the shapes of the CV curves, even at higher scan rates, indicating that the ASC device had a good transient-current response and capacitive performance [45]. Figure 7c displays the discharge curves, which illustrate the ASC's discharge performance as the current density gradually increased. The GCD curves obtained at diverse densities of current, from 1 to 20 A g<sup>-1</sup>, exhibited remarkable electrochemical reversibility, as evidenced by their excellent symmetry. Based on the GCD curves obtained at various current densities (as shown in Figure 7d), the device was found to exhibit a specific capacitance of up to 170 F g<sup>-1</sup> at a current density of 1 A g<sup>-1</sup>. Interestingly, even at a significantly higher current density of 20 A g<sup>-1</sup>, the specific capacitance was observed to remain constant at 55 F g<sup>-1</sup>. Figure 7e shows that the device's charge–discharge rate and power density can be improved, as the values obtained of electrochemical impedance spectroscopy (EIS) at the open circuit potential with an amplitude of 10 mV for the R<sub>s</sub> and the R<sub>ct</sub> of the NiSe@Ni/graphene||AC were 1.41 and 0.85 Ω, respectively, which were considered favorable. When the NiSe@Ni/graphene||AC device was detected at 10,000 charge–discharge cycles at a current density of 10 A g<sup>-1</sup>, the coulombic efficiency consistently remained above 98%, as shown in Figure 7e. However, the capacitance initially decreased significantly in the early cycles due to the loss of electrode capacity resulting from the electrolyte decomposition and the formation of an irreversible SEI layer [46]. After 2000 cycles, the

specific capacity of the NiSe@Ni/graphene electrode gradually increased. The device exhibited excellent long-term cycle stability, with a capacitance retention of 72.53% even after 10,000 cycles. The increase in specific capacity was primarily due to the reversible formation of a gel-like protective layer by the nanoparticles on the surface of the NiSe@Ni/graphene electrode, which exhibited “pseudocapacitive behavior”, which is commonly found in electrodes composed of graphene/transition-metal compounds [47]. These test results demonstrate that the NiSe@Ni/graphene//AC supercapacitor has good charge–discharge and cycle performance, and that it is an excellent energy-storage device. Figure 7f displays the Ragone plot of the device’s energy density and power density. The results show that the NiSe@Ni/graphene//AC asymmetric supercapacitor outperforms similar metal-selenide energy-storage devices [48–52], with a high energy density of 68 Wh kg<sup>-1</sup> at a power density of 853 W kg<sup>-1</sup> and an energy density of 22 Wh kg<sup>-1</sup> at a power density of 16,737 W kg<sup>-1</sup>.

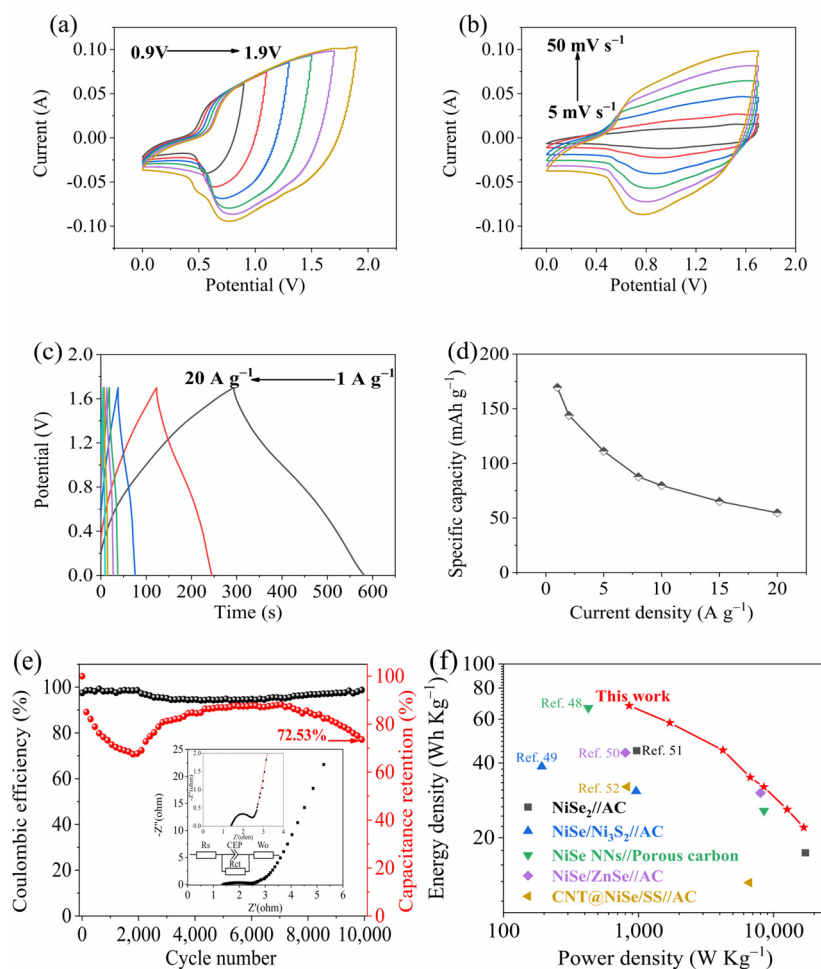


**Figure 7.** (a) CV curves obtained within different voltage windows. (b) CV curves recorded at various scan rates. (c) GCD curves measured at a current density of 1 A g<sup>-1</sup>. (d) Specific capacitance at different current densities. (e) Capacitance retention and coulombic efficiency (inset was the EIS plot). (f) Ragone plot.

**4. Conclusions**

Electroless nickel plating on graphene is an important step in the preparation of NiSe@Ni/graphene composites. Adjustments were made to the thickness and dispersion of the electroless nickel-plating layer on the surface of the graphene, as well as to the degree of defects present in the graphene. After obtaining an electroless nickel plating on 2D graphene sheets, selenization was performed. Throughout the reaction process, the Ni present in the

outer layer was initially transformed into NiSe through selenization. The metal nickel and NiSe nanoparticles that did not make full contact with the selenium-powder flow were intricately dispersed onto a 2D graphene sheet due to the variance in their grain sizes. As a result, they formed a 3D sandwich structure of NiSe@Ni/graphene. The material's ability to provide a greater number of active sites, its large specific surface area, and the unexpected synergistic effects that arose from the combination of the three materials collectively contributed to the material's high performance. Graphene and Ni exhibit superior electrical conductivity by leveraging the synergies between graphene, metallic nickel, and NiSe particles, while the remarkable electrochemical activity of NiSe further enhances the rate of the redox reaction. At a density of current of  $1 \text{ A g}^{-1}$ , the material exhibited a remarkable capacity of  $302 \text{ mAh g}^{-1}$  (equivalent to  $2716 \text{ F g}^{-1}$ ). Additionally, the material performed exceptionally well when assembled as a positive activated carbon and negative electrode in an asymmetric supercapacitor. At a density of current of  $1 \text{ A g}^{-1}$ , the device displayed a high capacity of  $170 \text{ F g}^{-1}$ , while maintaining a coulombic efficiency and capacity retention of 100% and 72.53%, respectively, over 10,000 cycles. The ASC device achieved high energy and power densities of  $68 \text{ Wh kg}^{-1}$  and  $16,737 \text{ W kg}^{-1}$ , respectively.

**Supplementary Materials:** The following supporting information can be downloaded at: <https://www.mdpi.com/article/10.3390/coatings13050885/s1>, Figure S1: The electrochemical parameters of the AC electrode: (a) CV curves. (b) GCD curves. (c) Specific capacities.; Table S1: Comparison between transition metal selenides and graphene composite of electrode materials.

**Author Contributions:** Conceptualization, J.J.; data curation, X.X., F.J., Z.P., P.Z., Z.W., H.Y. and J.J.; formal analysis, X.X., Z.P. and J.J.; methodology, X.X., F.J., Z.P., H.Y. and J.J.; resources, Z.P. and J.J.; writing—original draft preparation, X.X.; writing—review and editing, X.X., H.Y. and J.J. All authors have read and agreed to the published version of the manuscript.

**Funding:** The authors are grateful to the support by the Hong Liu First-Class Disciplines Development Program of Lanzhou University of Technology.

**Institutional Review Board Statement:** Not applicable.

**Informed Consent Statement:** Not applicable.

**Data Availability Statement:** Publicly available datasets were analyzed in this study. This data can be found here.

**Conflicts of Interest:** The authors declare no conflict of interest.

## References

1. Shan, X.; Zhang, S.; Zhang, N.; Chen, Y.; Gao, H.; Zhang, X. Synthesis and characterization of three-dimensional MoS<sub>2</sub>@carbon fibers hierarchical architecture with high capacity and high mass loading for Li-ion batteries. *J. Colloid Interface Sci.* **2018**, *510*, 327–333. [CrossRef] [PubMed]
2. Deng, W.; Kang, T.; Liu, H.; Zhang, J.; Wang, N.; Lu, N.; Ma, Y.; Umar, A.; Guo, Z. Potassium Hydroxide Activated and Nitrogen Doped Graphene with Enhanced Supercapacitive Behavior. *Sci. Adv. Mater.* **2018**, *10*, 937–949. [CrossRef]
3. Lai, R.; Shi, P.; Yi, Z.; Li, H.; Yi, Y. Triple-band surface plasmon resonance metamaterial absorber based on open-ended prohibited sign type monolayer graphene. *Micromachines* **2023**, *14*, 953. [CrossRef]
4. Ye, Z.; Wu, P.; Wang, H.; Jiang, S.; Huang, M.; Lei, D.; Wu, F. Multimode tunable terahertz absorber based on a quarter graphene disk structure. *Results Phys.* **2023**, *48*, 106420. [CrossRef]
5. Choudhary, N.; Li, C.; Moore, J.; Nagaiah, N.; Zhai, L.; Jung, Y.; Thomas, J. Asymmetric Supercapacitor Electrodes and Devices. *Adv. Mater.* **2017**, *29*, 1605336. [CrossRef]
6. Lv, S.; Ma, L.; Shen, X.; Tong, H. Recent design and control of carbon materials for supercapacitors. *J. Mater. Sci.* **2021**, *56*, 1919–1942. [CrossRef]
7. Santhosh, G.; Nayaka, G.P.; Bhatt, A.S. Ultrahigh capacitance of NiCo<sub>2</sub>O<sub>4</sub>/CeO<sub>2</sub> mixed metal oxide material for supercapacitor applications. *J. Alloys Compd.* **2022**, *899*, 163312. [CrossRef]
8. Shi, Z.; Zhu, J.; Li, Z.; Xiao, Q.; Zhu, J. Sulfur-Doped Nickel–Cobalt Double Hydroxide Electrodes for High-Performance Asymmetric Supercapacitors. *ACS Appl. Energy Mater.* **2020**, *3*, 11082–11090. [CrossRef]
9. Li, S.; Yang, Y.; Hu, Z.; Li, S.; Ding, F.; Xiao, X.; Si, P.; Ulstrup, J. Hetero-structured NiS<sub>2</sub>/CoS<sub>2</sub> nanospheres embedded on N/S co-doped carbon nanocages with ultra-thin nanosheets for hybrid supercapacitors. *Electrochim. Acta* **2022**, *424*, 140604. [CrossRef]

10. Senthilkumar, E.; Sivasankar, V.; Kohakade, B.R.; Thileepkumar, K.; Ramya, M.; Sivagaami Sundari, G.; Raghu, S.; Kalaivani, R.A. Synthesis of nanoporous graphene and their electrochemical performance in a symmetric supercapacitor. *Appl. Surf. Sci.* **2018**, *460*, 17–24. [[CrossRef](#)]
11. Lee, S.; Cho, M.S.; Lee, H.; Nam, J.-D.; Lee, Y. A facile synthetic route for well defined multilayer films of graphene and PEDOT via an electrochemical method. *J. Mater. Chem.* **2012**, *22*, 1899–1903. [[CrossRef](#)]
12. Zhang, H.; Wang, K.; Zhang, X.; Lin, H.; Sun, X.; Li, C.; Ma, Y. Self-generating graphene and porous nanocarbon composites for capacitive energy storage. *J. Mater. Chem. A* **2015**, *3*, 11277–11286. [[CrossRef](#)]
13. Karaman, C.; Bayram, E.; Karaman, O.; Aktaş, Z. Preparation of high surface area nitrogen doped graphene for the assessment of morphologic properties and nitrogen content impacts on supercapacitors. *J. Electroanal. Chem.* **2020**, *868*, 114197. [[CrossRef](#)]
14. Zhang, Y.; Zou, Q.; Hsu, H.S.; Raina, S.; Xu, Y.; Kang, J.B.; Chen, J.; Deng, S.; Xu, N.; Kang, W.P. Morphology Effect of Vertical Graphene on the High Performance of Supercapacitor Electrode. *ACS Appl. Mater. Interfaces* **2016**, *8*, 7363–7369. [[CrossRef](#)]
15. Zheng, X.; Jiang, J.; Bi, T.; Jin, F.; Li, M. FeCo<sub>2</sub>S<sub>4</sub>@Ni/graphene Nanocomposites with Rich Defects Induced by Heterointerface Engineering for High-Performance Supercapacitors. *ACS Appl. Energy Mater.* **2021**, *4*, 3288–3296. [[CrossRef](#)]
16. Zheng, X.; He, X.; Jiang, J.; Jia, Z.; Li, Y.; Wei, Z.; Yang, H. High-Performance Asymmetric Supercapacitors Based on the Ni<sub>1.5</sub>Co<sub>1.5</sub>S<sub>4</sub>@CNTs Nanocomposites. *Nano* **2020**, *15*, 2050136. [[CrossRef](#)]
17. Theerthagiri, J.; Karuppasamy, K.; Durai, G.; Rana, A.U.H.S.; Arunachalam, P.; Sangeetha, K.; Kuppasami, P.; Kim, H.-S. Recent Advances in Metal Chalcogenides (MX<sub>2</sub>; X = S, Se) Nanostructures for Electrochemical Supercapacitor Applications: A Brief Review. *Nanomaterials* **2018**, *8*, 256. [[CrossRef](#)]
18. Zhao, L.; Zhang, P.; Zhang, Y.; Zhang, Z.; Yang, L.; Chen, Z.-G. Facile synthesis of hierarchical Ni<sub>3</sub>Se<sub>2</sub> nanodendrite arrays for supercapacitors. *J. Mater. Sci. Technol.* **2020**, *54*, 69–76. [[CrossRef](#)]
19. Bai, Y.; Shen, W.; Song, K.; Zhang, S.; Wang, Y.; Xu, T.; Xu, J.; Dai, S.; Wang, X. Controlled synthesis of NiSe-Ni<sub>0.85</sub>Se nanocomposites for high-performance hybrid supercapacitors. *J. Electroanal. Chem.* **2021**, *880*, 114795. [[CrossRef](#)]
20. Arai, S.; Suzuki, Y.; Nakagawa, J.; Yamamoto, T.; Endo, M. Fabrication of metal coated carbon nanotubes by electroless deposition for improved wettability with molten aluminum. *Surf. Coat. Technol.* **2012**, *212*, 207–213. [[CrossRef](#)]
21. Bi, T.; Jiang, J.; Lei, Y.; Zheng, X.; Jia, Z.; Wei, Z.; Yang, H. Improving supercapacitive performance of CNTs/NiCo<sub>2</sub>S<sub>4</sub> composites by interface regulation. *Appl. Surf. Sci.* **2020**, *530*, 147317. [[CrossRef](#)]
22. Lupi, C.; Dell’Era, A.; Pasquali, M. Effectiveness of sodium citrate on electrodeposition process of NiCoW alloys for hydrogen evolution reaction. *Int. J. Hydrogen Energy* **2017**, *42*, 28766–28776. [[CrossRef](#)]
23. López, J.R.; Flores, L.; Méndez, P.F.; Bueno, J.J.P.; Trejo, G.; Meas, Y. Effect of Boric Acid, Sodium Nitrate, and Sodium Dodecyl Sulfate as Additives on the Hydrogen Permeation during Nickel Electroplating on Palladium Electrodes. *J. Electrochem. Soc.* **2021**, *168*, 062516. [[CrossRef](#)]
24. Jin, F.; Li, M.; Xie, L.; Jiang, J. Selenium-doped carbon nanotubes/nickel selenide coaxial nanocables for energy storage. *J. Power Sources* **2021**, *514*, 230587. [[CrossRef](#)]
25. Shao, Y.; El-Kady, M.F.; Sun, J.; Li, Y.; Zhang, Q.; Zhu, M.; Wang, H.; Dunn, B.; Kaner, R.B. Design and Mechanisms of Asymmetric Supercapacitors. *Chem. Rev.* **2018**, *118*, 9233–9280. [[CrossRef](#)]
26. Xie, L.; Li, M.; Zhu, P.; Xiao, X.; Jia, Z.; Wei, Z.; Jiang, J. Novel combination of nickel-cobalt sulfide and oxide derived from Ni<sub>2</sub>CoS<sub>4</sub>@ZIF-67 for high performance supercapacitor. *J. Alloys Compd.* **2022**, *898*, 162861. [[CrossRef](#)]
27. Cheng, T.; Gao, H.; Liu, G.; Pu, Z.; Wang, S.; Yi, Z.; Wu, X.; Yang, H. Preparation of core-shell heterojunction photocatalysts by coating CdS nanoparticles onto Bi<sub>4</sub>Ti<sub>3</sub>O<sub>12</sub> hierarchical microspheres and their photocatalytic removal of organic pollutants and Cr(VI) ions. *Colloids Surf. A Physicochem. Eng. Asp.* **2022**, *633*, 127918. [[CrossRef](#)]
28. Gu, Y.; Guo, B.; Yi, Z.; Wu, X.; Zhang, J.; Yang, H. Synthesis of a Self-assembled Dual Morphologies Ag-NPs/SrMoO<sub>4</sub> Photocatalyst with LSPR Effect for the Degradation of Methylene Blue Dye. *ChemistrySelect* **2022**, *7*, e202201274. [[CrossRef](#)]
29. Wu, X.T.; Yin, C.S.; Zhang, M.F.; Xie, Y.Q.; Hu, J.J.; Long, R.L.; Wu, X.M.; Wu, X.W. The intercalation cathode of MOFs-driven vanadium-based composite embedded in N-doped carbon for aqueous zinc ion batteries. *Chem. Eng. J.* **2023**, *452*, 139573. [[CrossRef](#)]
30. Wu, X.S.; Zhang, Z.; He, C.; Shen, Y.; Wu, X.; Wang, H.; Ma, Z.; Li, Q. Mixed-valence cobalt oxides bifunctional electrocatalyst with rich oxygen vacancies for aqueous metal-air batteries. *Chem. Eng. J.* **2023**, *453*, 139831. [[CrossRef](#)]
31. Li, L.; Sun, X.; Xian, T.; Gao, H.; Wang, S.; Yi, Z.; Wu, X.; Yang, H. Template-free synthesis of Bi<sub>2</sub>O<sub>2</sub>CO<sub>3</sub> hierarchical nanotubes self-assembled from ordered nanoplates for promising photocatalytic applications. *Phys. Chem. Chem. Phys.* **2022**, *24*, 8279–8295. [[CrossRef](#)]
32. Subhadarshini, S.; Pavitra, E.; Rama Raju, G.S.; Chodankar, N.R.; Goswami, D.K.; Han, Y.-K.; Huh, Y.S.; Das, N.C. One-Dimensional NiSe–Se Hollow Nanotubular Architecture as a Binder-Free Cathode with Enhanced Redox Reactions for High-Performance Hybrid Supercapacitors. *ACS Appl. Mater. Interfaces* **2020**, *12*, 29302–29315. [[CrossRef](#)]
33. Liu, Y.; Zheng, Y.; Xu, Q.; Shi, Y.; Tian, Z.; Wang, R.; Zhang, G.; Chen, J.; Wang, Z.; Zheng, W. Controllable synthesis of NiSe/MoSe<sub>2</sub>/MoO<sub>2</sub> 3D hierarchical hollow microspheres with enhanced performance for asymmetric supercapacitors. *Chem. Eng. J.* **2020**, *387*, 124121. [[CrossRef](#)]
34. Wu, H.; Lu, X.; Zheng, G.; Ho, G.W. Topotactic Engineering of Ultrathin 2D Nonlayered Nickel Selenides for Full Water Electrolysis. *Adv. Energy Mater.* **2018**, *8*, 1702704. [[CrossRef](#)]

35. Sun, Y.-Y.; Zhu, Y.-X.; Wu, L.-K.; Hou, G.-Y.; Tang, Y.-P.; Cao, H.-Z.; Zheng, G.-Q. Hierarchical NiSe@Ni nanocone arrays electrocatalyst for oxygen evolution reaction. *Electrochim. Acta* **2020**, *353*, 136519. [[CrossRef](#)]
36. Zhu, Y.; Huang, Z.; Hu, Z.; Xi, L.; Ji, X.; Liu, Y. 3D interconnected ultrathin cobalt selenide nanosheets as cathode materials for hybrid supercapacitors. *Electrochim. Acta* **2018**, *269*, 30–37. [[CrossRef](#)]
37. Zhang, X.; Zhen, M.; Bai, J.; Jin, S.; Liu, L. Efficient NiSe-Ni<sub>3</sub>Se<sub>2</sub>/Graphene Electrocatalyst in Dye-Sensitized Solar Cells: The Role of Hollow Hybrid Nanostructure. *ACS Appl. Mater. Interfaces* **2016**, *8*, 17187–17193. [[CrossRef](#)]
38. Zhang, X.; Jing, T.-z.; Guo, S.-q.; Gao, G.-d.; Liu, L. Synthesis of NiSe<sub>2</sub>/reduced graphene oxide crystalline materials and their efficient electrocatalytic activity in dye-sensitized solar cells. *RSC Adv.* **2014**, *4*, 50312–50317. [[CrossRef](#)]
39. Dong, L.; Gari, R.R.S.; Li, Z.; Craig, M.M.; Hou, S. Graphene-supported platinum and platinum–ruthenium nanoparticles with high electrocatalytic activity for methanol and ethanol oxidation. *Carbon* **2010**, *48*, 781–787. [[CrossRef](#)]
40. Li, C.P.; Shi, X.D.; Liang, S.Q.; Ma, X.M.; Han, M.M.; Wu, X.W.; Zhou, J. Spatially homogeneous copper foam as surface dendrite-free host for zinc metal anode. *Chem. Eng. J.* **2020**, *379*, 122248. [[CrossRef](#)]
41. Gogotsi, Y.; Penner, R.M. Energy Storage in Nanomaterials—Capacitive, Pseudocapacitive, or Battery-like? *ACS Nano* **2018**, *12*, 2081–2083. [[CrossRef](#)] [[PubMed](#)]
42. Tkach, A. Graphene/Reduced Graphene Oxide-Carbon Nanotubes Composite Electrodes: From Capacitive to Battery-Type Behaviour. *Nanomaterials* **2021**, *11*, 1240. [[CrossRef](#)]
43. Xu, X.; Zhang, Z.; Xiong, R.; Lu, G.; Zhang, J.; Ning, W.; Hu, S.; Feng, Q.; Qiao, S. Bending Resistance Covalent Organic Framework Superlattice: “Nano-Hourglass”-Induced Charge Accumulation for Flexible In-Plane Micro-Supercapacitors. *Nano-Micro Lett.* **2022**, *15*, 25. [[CrossRef](#)] [[PubMed](#)]
44. Wang, X.; Yan, C.; Sumboja, A.; Lee, P.S. High performance porous nickel cobalt oxide nanowires for asymmetric supercapacitor. *Nano Energy* **2014**, *3*, 119–126. [[CrossRef](#)]
45. Yan, M.; Yao, Y.; Wen, J.; Long, L.; Kong, M.; Zhang, G.; Liao, X.; Yin, G.; Huang, Z. Construction of a Hierarchical NiCo<sub>2</sub>S<sub>4</sub>@PPy Core-Shell Heterostructure Nanotube Array on Ni Foam for a High-Performance Asymmetric Supercapacitor. *ACS Appl. Mater. Interfaces* **2016**, *8*, 24525–24535. [[CrossRef](#)]
46. Zhou, Y.; Tian, R.; Duan, H.; Wang, K.; Guo, Y.; Li, H.; Liu, H. CoSe/Co nanoparticles wrapped by in situ grown N-doped graphitic carbon nanosheets as anode material for advanced lithium ion batteries. *J. Power Sources* **2018**, *399*, 223–230. [[CrossRef](#)]
47. Gauthier, M.; Carney, T.J.; Grimaud, A.; Giordano, L.; Pour, N.; Chang, H.-H.; Fenning, D.P.; Lux, S.F.; Paschos, O.; Bauer, C.; et al. Electrode–Electrolyte Interface in Li-Ion Batteries: Current Understanding and New Insights. *J. Phys. Chem. Lett.* **2015**, *6*, 4653–4672. [[CrossRef](#)]
48. Yu, D.; Li, Z.; Zhao, G.; Zhang, H.; Aslan, H.; Li, J.; Sun, F.; Zhu, L.; Du, B.; Yang, B.; et al. Porous Ultrathin NiSe Nanosheet Networks on Nickel Foam for High-Performance Hybrid Supercapacitors. *ChemSusChem* **2020**, *13*, 260–266. [[CrossRef](#)]
49. Ye, B.; Gong, C.; Huang, M.; Ge, J.; Fan, L.; Lin, J.; Wu, J. A high-performance asymmetric supercapacitor based on Ni<sub>3</sub>S<sub>2</sub>-coated NiSe arrays as positive electrode. *New J. Chem.* **2019**, *43*, 2389–2399. [[CrossRef](#)]
50. Ye, B.; Cao, X.; Zhao, Q.; Wang, J. Coelectrodeposition of NiSe/ZnSe Hybrid Nanostructures as a Battery-Type Electrode for an Asymmetric Supercapacitor. *J. Phys. Chem. C* **2020**, *124*, 21242–21249. [[CrossRef](#)]
51. Wang, S.; Li, W.; Xin, L.; Wu, M.; Long, Y.; Huang, H.; Lou, X. Facile synthesis of truncated cube-like NiSe<sub>2</sub> single crystals for high-performance asymmetric supercapacitors. *Chem. Eng. J.* **2017**, *330*, 1334–1341. [[CrossRef](#)]
52. Chen, T.-Y.; Vedhanarayanan, B.; Lin, S.-Y.; Shao, L.-D.; Sofer, Z.; Lin, J.-Y.; Lin, T.-W. Electrodeposited NiSe on a forest of carbon nanotubes as a free-standing electrode for hybrid supercapacitors and overall water splitting. *J. Colloid Interface Sci.* **2020**, *574*, 300–311. [[CrossRef](#)]

**Disclaimer/Publisher’s Note:** The statements, opinions and data contained in all publications are solely those of the individual author(s) and contributor(s) and not of MDPI and/or the editor(s). MDPI and/or the editor(s) disclaim responsibility for any injury to people or property resulting from any ideas, methods, instructions or products referred to in the content.